Modulation of post-fracture roughness with induced shear stress in the smart cut process

Lucas Colonel, Q. Lomonaco, K. Abadie, L G Michaud, C. Morales, S. Moreau, F. Mazen, F. Fournel, D. Landru, F. Rieutord

Journal of Applied Physics

RESEARCH ARTICLE | JULY 22 2024

Modulation of post-fracture roughness with induced shear stress in the smart cut process

Lucas Colonel ; Q. Lomonaco ; K. Abadie ; L. G. Michaud ; C. Morales; S. Moreau ; F. Mazen ; F. Fournel ; D. Landru ; F. Rieutord

J. Appl. Phys. 136, 045106 (2024)
https://doi.org/10.1063/5.0223114

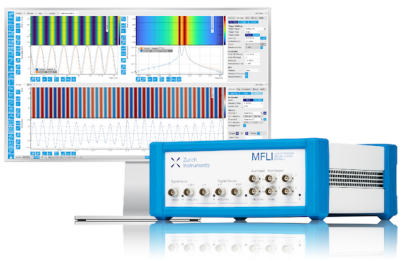

Journal of Applied Physics ARTICLE pubs.aip.org/aip/jap

Modulation of post-fracture roughness with induced shear stress in the smart cut process

Cite as: J. Appl. Phys. **136**, 045106 (2024); doi: 10.1063/5.0223114
Submitted: 12 June 2024 · Accepted: 3 July 2024 ·
Published Online: 22 July 2024

Lucas Colonel,[1,a)] Q. Lomonaco,[1] K. Abadie,[1] L. G. Michaud,[2] C. Morales,[1] S. Moreau,[1] F. Mazen,[1] F. Fournel,[1] D. Landru,[3] and F. Rieutord[3]

AFFILIATIONS

[1]Université Grenoble Alpes, CEA, LETI, F-38000 Grenoble, France
[2]EV Group, DI E. Thallner Straße 1, 4782 St. Florian/Inn, Austria
[3]SOITEC, Parc Technologique des Fontaines, 38190 Bernin, France

[a)]**Author to whom correspondence should be addressed:** lucas.colonel@cea.fr

ABSTRACT

Surface pattern formation of Smart Cut™ silicon-on-insulator (SOI) substrates is investigated using a new process derived from this technology. The local control of SOI surface roughness is achieved by using hetero-temperature surface activated bonding to introduce locally bespoke shear stresses into bonded silicon wafers. The finite element method is used to back up experimental measurements of these large deformations to determine the amount of shear stresses introduced into the structure, and to determine its impact on the fracture mechanism.

I. INTRODUCTION

The fracture of brittle materials, like crystalline silicon, has been extensively studied in the literature.[1–3] Fracture understanding and control is a key step in the maturity of the Smart Cut™ technology for silicon-on-insulator (SOI) production.[4] This process consists of implanting a high dose of light gas ions in a layer-donor substrate which is then assembled to a host receiver-substrate, typically using direct bonding techniques.[5,6] Bonded wafers are then annealed up to a fracture event occurring at the depth of implanted species, leading to the transfer of the top layer from the donor onto the receiver.

Numerous studies in the literature have focused on the annealing stage leading to fracture in the Smart Cut process, with attention being paid to implanted defects growth,[7] species diffusion,[8] and cracks coalescence [Fig. 1(a)].[9] However, Smart Cut fracture annealing ends up with the spontaneous propagation of a macroscopic crack through the whole assembly.[10] Fractured surfaces exhibit an inherent roughness which originates from both defect growth history and deviations of the final fracture path.[11] [Fig. 1(b)]

Previous works by Landru *et al.*[11] and Massy *et al.*[12] focused on the origin of long wavelength surface patterns observed on the SOI surface [Fig. 1(b)]. Their work showed that these patterns are local variations in roughness formed by the interaction of acoustic waves emitted by the fracture and reflected in the substrates with this same fracture front [Fig. 1(b)].[13] In this case, the variation in roughness seems to be related to the sensitivity of the crack path to the shear stresses induced by the acoustic waves.

Consequently, shear stresses must be taken into account to understand properly these phenomena. In this paper, a new approach is explored to introduce shear stresses prior to fracture annealing, using the hetero-temperature surface activated bonding (HT-SAB) process,[14] aiming to determine the influence of stresses on SOI surface roughness.

II. EXPERIMENTAL PROCESS AND CONDITIONS

A Smart Cut like process was carried to produce eight implanted and bonded silicon structures, with consequent stresses generated at the bonding interface. The following novel flow chart was adopted to produce these samples (Fig. 2).The donor 200 mm Si(001) wafer was prepared (before bonding) with He and H ion implantation in reference conditions [Fig. 2(i)].[15] Then, the host Si(001) wafer was thermally annealed to reach a 350 nm thick

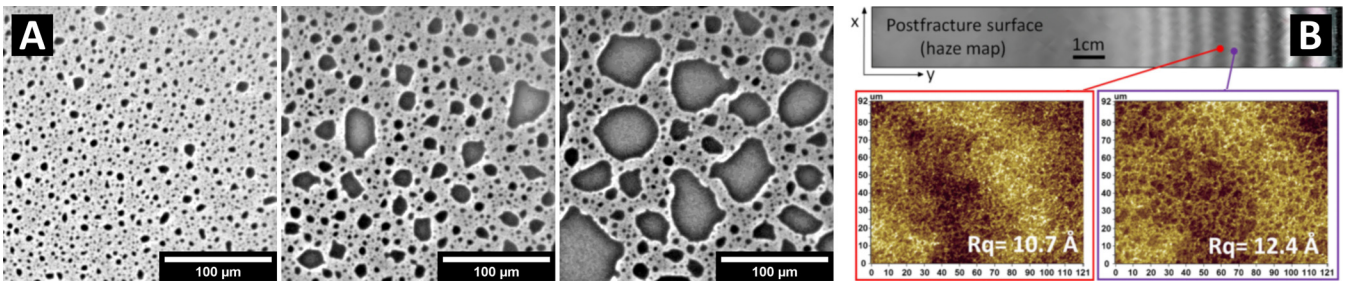

FIG. 1. (a) IR confocal images of microcrack growth, from the limit of detection up to splitting during a Smart Cut process [adapted with permission from Colonel *et al.*, Phys. Status Solidi A **218**, 2100219 (2021). Copyright 2021 Wiley VCH]. (b) Fracture wake pattern on a SOI surface and the corresponding optical interferometer images of bright and dark fringes [adapted with permission from Massy *et al.*, Phys. Rev. Lett. **121**, 195501 (2018). Copyright 2018 APS].

oxide layer [Fig. 2(ii)]. A 40 nm bonding layer of amorphous silicon was then deposited using LPCVD technique [Fig. 2(iii)].

Finally, both donor and host substrates were bonded together using a specific use of surface activated bonding (SAB) technique [Fig. 2(iv)]. Indeed, room temperature covalent bonding can be achieved for metals or semi-conductors in an ultra-high vacuum (UHV) environment (about 10^{-6} Pa) after the removal of native oxides and surface contaminants.[16,17] Substrate surfaces to be bonded are pre-treated in an activation chamber using ionic argon beam bombardment [Fig. 2iv(a)]. Ballistic impacts remove the surface native oxide enabling free surface dangling bonds on the material surface. These dangling bonds are not passivated under UHV, resulting in an extremely reactive surface for bonding[18] and no post-bonding annealing are needed with such a technique. Covalent bonding in UHV is thus mainly devoted to room temperature bonding. However, as shown by Abadie *et al.*,[19] high temperature bonding above 200 °C is feasible (both wafers at the same temperature). The dangling bonds do not seem to be passivated faster in the UHV by heating the wafer or not.

However, in this work, SAB technique was used to trap and introduce on purpose stresses in bonded structures. The manufacturing of stressed stacks by hetero-temperature bonding was based on previous works by Lomonaco *et al.*[14] In order to introduce stresses in the pre-SOI bonded structure prior to fracture, the HT-SAB technique is employed to produce stacks with a bonding temperature differential T_{Top} and T_{Bottom} between the two substrates [Fig. 2iv(b)]. Because of the coefficient of thermal expansion (CTE) of crystalline silicon,[20] different expansions of Si substrates were achieved in the bonding machine EVG® Combond®. This process results in internal stress introduction, with in a large

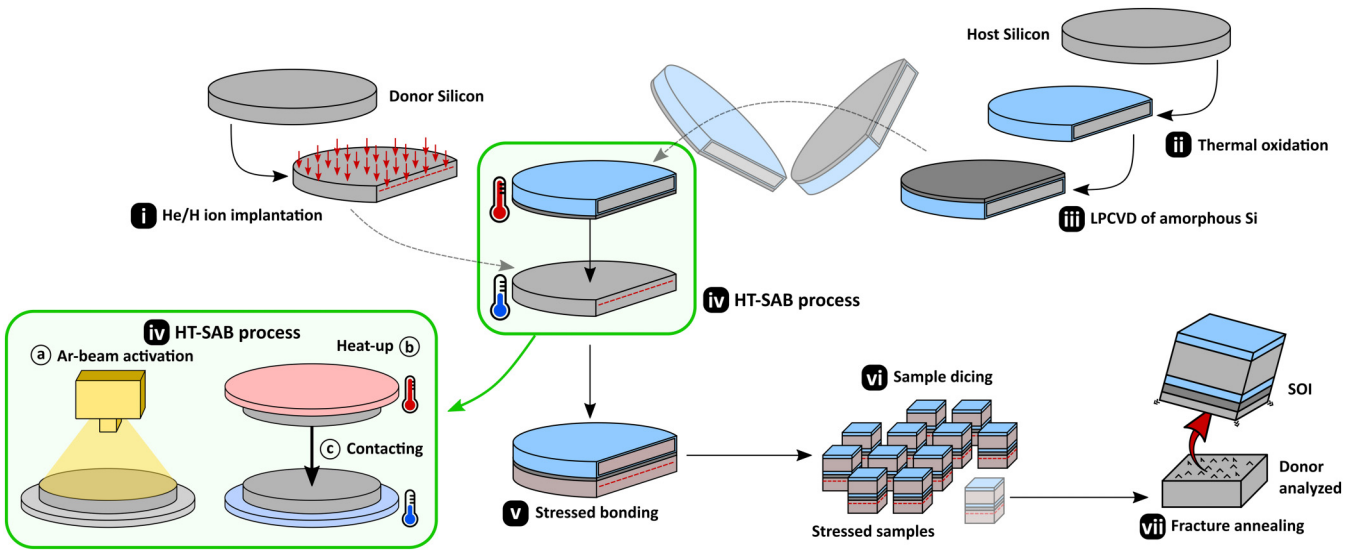

FIG. 2. Smart Cut like flow chart performed to introduce stresses during bonding, prior to the silicon fracture. The bonding scheme is a simplified representation of the EVG® Combond® system used for this experiment. Heating chuck temperatures are independently monitored.

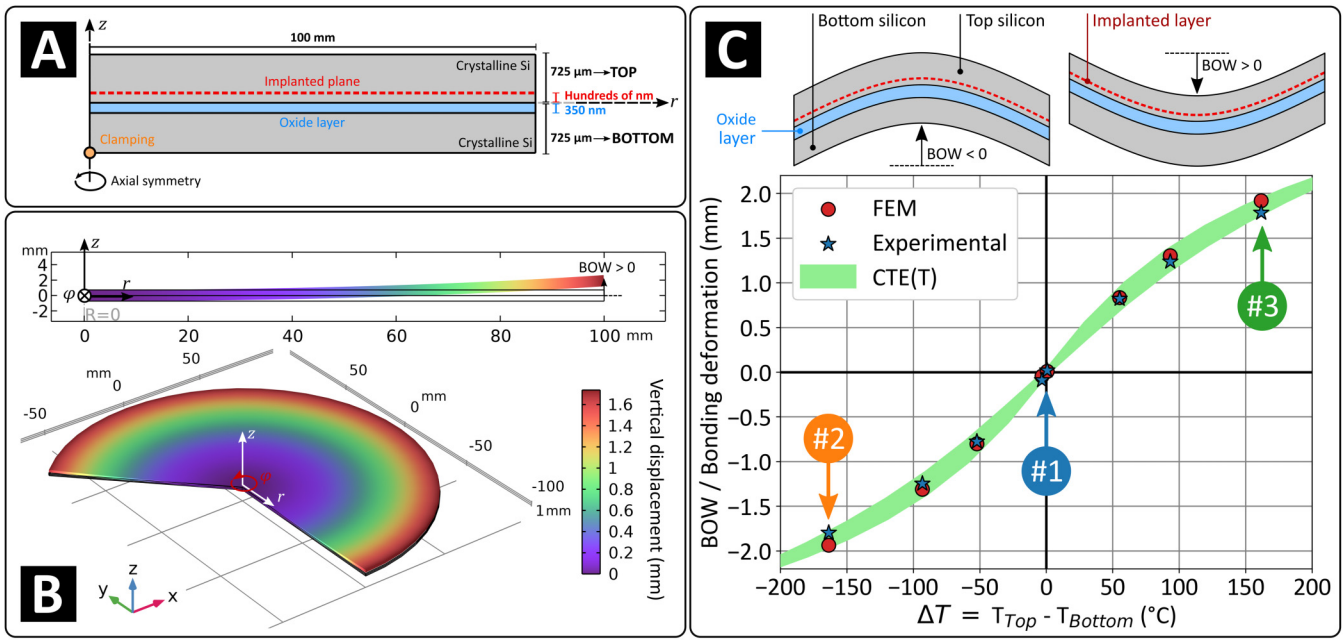

FIG. 3. (a) Considered structure and geometry used for the FEM. (b) 2D and 3D representation of simulated vertical displacement with $\Delta T = 161.6$ °C. (c) Experimental and numerical bonding deformation (i.e., bow) as functions of bonding temperature differential ΔT and schematics depending on the bow sign.

deformation (i.e., bow) of stacked wafers when the two substrates recover the same temperature even if both substrates are made of the same material [Fig. 2(v)].

Since large displacements are reached during this process,[14,21] no analytical model is suitable for describing this stressed structure and determine shear stress values. Therefore, a convenient way to predict wafer deformations (i.e., wafer bow) was to use the finite element method (FEM). A numerical modeling of the hetero-temperature bonding was carried out using COMSOL Multiphysics® and its Structural Mechanics Module.[22] For this purpose, a 2D axisymmetric model of 200 mm bonded silicon wafers is built [Fig. 3(a)]. At the central bottom point with $r = 0$, the vertical displacement is fixed at zero.

Then, a static non-linear analysis was performed in linear elastic conditions. To mimic the hetero-temperature covalent bonding process, bottom and top wafers were initially thermally expanded according to T_{Bottom} and T_{Top}. Then, expanded wafers were assembled, and the structure was brought back to room temperature. The vertical displacement of the wafer's edge was then extracted as shown in the example in Fig. 3(b) depicting a HT-SAB process carried out with $\Delta T = 161.6$ °C, resulting in a maximum displacement of approximately 1.9 mm.

Finally, temperature differences $\Delta T = T_{Top} - T_{Bottom}$ were set approximately in the ±160 °C range feasible with the bonding equipment to produce eight bonded structure (Table I). Each bonding is then carefully diced in $1 \times 1\,cm^2$ samples [Fig. 2(vi)] to perform multiple fine fracture analysis upon annealing [Fig. 2(vii)]. Note that cutting such structures into samples changes the internal shear stress distributions near the sample edges but do not relax them.

III. RESULTS, MODELS, AND DISCUSSIONS

The displacement (i.e., bow deformation) of such bonded structures were measured, at room temperature, with a FRT Microprof® equipment according to the SEMI standard[23] and were compared with the numerical simulation results (Table I) [Fig. 3(c)] demonstrating good matching results around 5% error, except for samples with small ΔT where the initial silicon wafer bowing is probably the cause of this large error.

It is important to note that due to silicon's CTE non-linearity, the impact of the ΔT position inside the bonding

TABLE I. Bonding temperatures with measured and simulated deformations. Colors correspond to further images.

Sample Nos.	T_{Top} (°C)	T_{Bottom} (°C)	ΔT (°C)	SEMI bow (mm)	FEM bow (mm)	Error (%)
1 (reference)	23.3	26.6	−3.3	−0.09	−0.04	55.6
2	94.3	258.0	−163.7	−1.80	−1.94	7.8
3	257.6	96.0	161.6	1.78	1.92	7.9
4	102.8	102.2	0.6	0.02	0.01	50.0
5	105.8	199.1	−93.3	−1.25	−1.31	4.8
6	198.2	105.1	93.1	1.24	1.31	5.6
7	98.9	151.2	−52.3	−0.78	−0.80	2.6
8	153.3	98.2	55.1	0.82	0.84	2.4

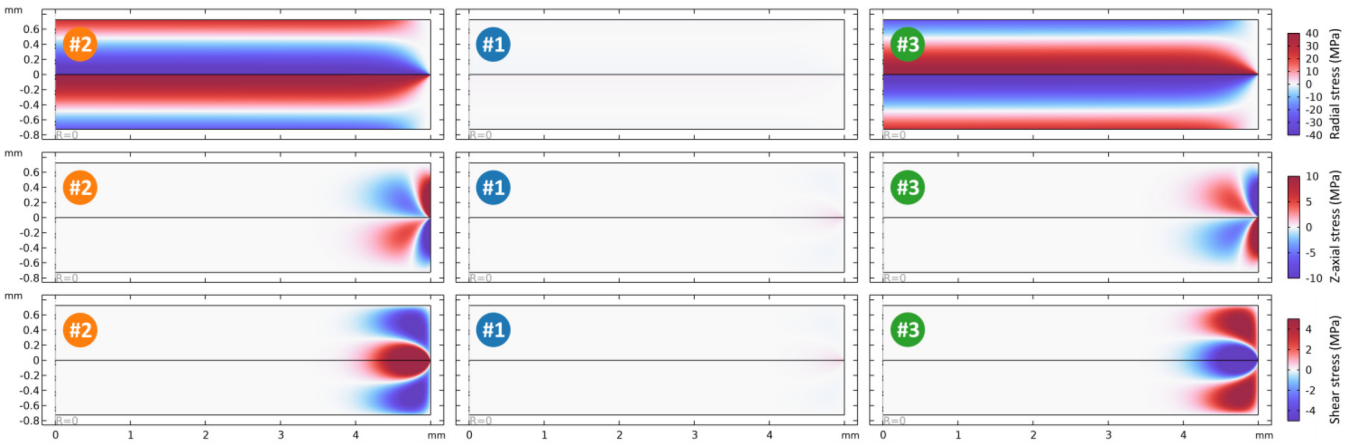

FIG. 4. FEM 2D radial cross-sectional view of each stress component for samples 2, 1, and 3 sorted in columns. The first, second, and third rows represent, respectively, radial, Z-axial and shear stresses in MPa for each sample.

temperature range [20, 260] °C is not negligible. The green curve bundle shown in Fig. 3(c) illustrates such a phenomena. The quite good correlation between experimental (blue stars) and numerical (red dots) measure shown in Fig. 3(c) enables us to: (i) validate the FEM and (ii) extract stresses from experimental displacement measurements in particularly near the wafer edge (where shear stresses rise).

To simplify and sum-up, only the reference sample #1, and samples with extreme temperature differences ΔT 2 and 3 (Table I) will be considered in the remainder of this paper.

Considering now $1 \times 1\,\mathrm{cm}^2$ sample sizes, the FE simulations are performed again in experimental condition of samples 1–3 to extract stress components. Cross-sectional views of each stress components are presented in Fig. 4. Simulation results show a uniform radial stresses σ_r near the implanted layers [Fig. 3(a)] of our samples close to ±40 MPa for samples 2 and 3. This radial stress is constant as long as edge effects are ignored, which is a good approximation when distance to edge is larger than wafer thickness $725\,\mu$m as shown on the first row in Fig. 4. Almost non-existent in the center, stresses along the z axis σ_z reach about ±30 MPa—so

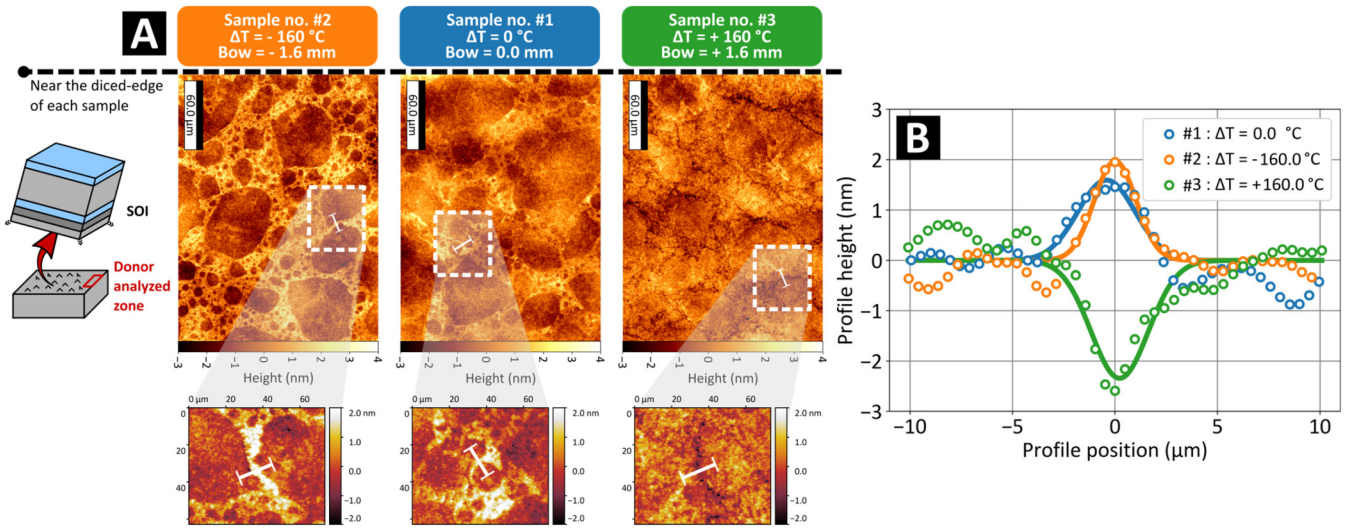

FIG. 5. (a) Optical interferometry images of the post-fracture surface at the edge of each sample (top of each image) and zooms on extracted profiles. (b) Typical profiles between marbling extracted from smoothed surface (dots) and corresponding Gaussian fits (lines). Profiles are centered on the deviation maxima.

TABLE II. Statistical roughness values: maximum height (S_z), arithmetical mean height (S_a), root mean square height (S_q), skewness (S_{sk}), and kurtosis (S_{ku}) for the three samples 1–3.

Sample Nos.	S_z (nm)	S_a (nm)	S_q (nm)	S_{sk}	S_{ku}
1 (reference)	6.43	0.59	0.74	0.34	0.24
2	7.19	0.73	0.90	0.41	−0.13
3	9.74	0.55	0.70	−0.11	0.39

tensile or compressive—close to the sample edge as presented on the second row in Fig. 4. Finally, edge displacements produce diverging shear stresses σ_{rz} up to ±5 MPa suspected to influence fracture roughness in the Smart Cut process according to Massy *et al.*[13] as depicted in the third row in Fig. 4.

Finally, samples 1–3 are annealed upon 400 °C in isothermal conditions up to the spontaneous fracture propagation to investigate the impact of edge shear stresses on the newly created surface of SOI substrates.

Surface topologies of each donor sample 1–3 are imaged by white light interferometry using a Bruker ContourGT-X® equipment in the phase-shift interferometry mode. The typical micrometre-scale surface roughness corresponding to the crack size previously observed, right before fracture propagation [Fig. 1(a)] could be measured. Note that for each sample, only the donor surface is characterized to avoid layer-stack interference with white light on SOI surface and only surface edges are considered given the presence of consistent shear stresses.

Samples surface images are presented in Fig. 5(a), where each sample edge is located on the top. Patterns are different. The surface of the reference sample 1—without stress—shows similarities with the literature [Fig. 1(b)].[13] This typical Smart Cut pattern presents fracture deviations slightly oriented toward the buried oxide layer as shown in Fig. 5(b).[13]

However, induced shear stresses have a strong impact on the fracture deviation amplitude and orientation. Pattern deviation is amplified for sample 2. Indeed, the slight orientation observed in sample 1 is more obvious and frequent for sample 2 [Fig. 5(a)] but also majorly higher [Fig. 5(b)]. On the other hand, sample 3 shows a clear pattern deletion [Fig. 5(a)] with often an orientation opposite to that of reference 1 [Fig. 5(b)].

Statistical roughness measurements, shown in Table II, tend to confirm previous observations. Indeed, the skewness parameter (S_{sk}) is the most significant here to describe marbling pattern orientations. A typical positive sign (samples 1 and 2) implies deviations in the form of peaks, while a negative sign (sample 3) implies deviations in the form of holes between the crack footprints. Finally, shear stress does not seem to clearly impact root mean square roughness (S_q) and other statistical parameters (Table II).

Shear stress in the material prior to fracture propagation seems to be the cause of such results. The FEM shear stress in the

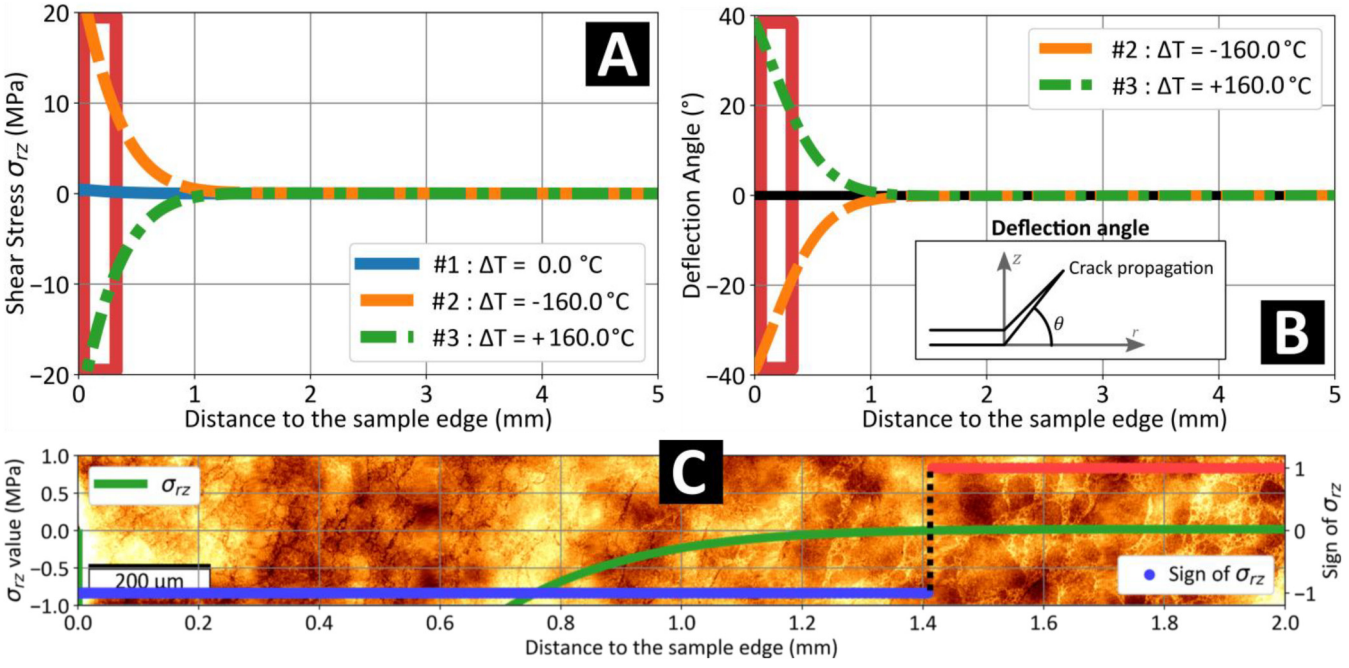

FIG. 6. (a) Simulated shear stress σ_{rz} in the implanted layer as a function of the distance to the sample edge (up to the center) for the three samples considered. The red square represents the observed length in Fig. 5(a). (b) Calculated deflection angle as a function of the distance to the sample edge (up to the center). The red square represents the observed length in Fig. 5(a). (c) Superposition of the interferometric image at the edge of sample 3 with the local shear stress value σ_{rz} (green) in the implanted plane and its sign (blue for negative values, red for positives). The dotted black line marks the change of sign.

fracture plane (i.e., implanted interface) is plotted as a function of the distance to the sample edge in Fig. 6(a). In this figure, a red-contour square defines the first 320 μm of the surface observed as shown in Fig. 5(a).

It appears that shear stresses close to sample edges—with values up to dozens of mega-Pascal—are in the same range than inner crack pressures given by the Griffith criterion and mechanical equilibrium.[24] Therefore, the Erdogan–Sih criterion enables the evaluation of the deflection angle θ [illustrated in Fig. 6(b)] adopted by the fracture as it propagates between cracks.[25] This so called "kink angle" can be determined using the values of stress intensity factors for modes I, K_I, and II, K_{II}, as follows [Eq. (1)]:

$$\theta = 2\text{artan}\left[\frac{1}{4}\left(\frac{K_I}{K_{II}} - \text{sign}(K_{II})\sqrt{8 + \left(\frac{K_I}{K_{II}}\right)^2}\right)\right]. \quad (1)$$

First, we can assume that the edge shear stress divergence behavior observed in simulations is indeed present. Let us consider a circular penny-shaped crack[26] with a radius R of about 10 μm, at its Griffith crack opening equilibrium[24] and positioned along the layer located at a variable distance r from the center. Using Eq. (2) equations, stress intensity factors K_I and K_{II} values can be calculated as

$$\begin{cases} K_I(R) = \dfrac{2}{\pi}\sigma_z\sqrt{\pi R} = P(R)\sqrt{\pi R}, \\ K_{II}(R) = \tau(r)\sqrt{\pi R} = \sigma_{rz}^{\text{FEM}}(R)\sqrt{\pi R}, \end{cases} \quad (2)$$

using $\tau(r)$, the shear stress in the implanted layer, taken from σ_{rz} component in the FEM simulations as shown in Fig. 6(a). Finally, the values of the deflection angle (i.e., the fracture deviation orientation) for each of the samples as a function of the crack position along the implanted layer—particularly close to the edge—can be calculated [Fig. 6(b)].

These calculations highlight that deflection angles change signs close to the sample edge, with a positive deflection for sample 3 and a negative one for sample 2 [Fig. 6(b)]. This result explains the marbling increase close to the edge of sample 2 and the deviation inversion for sample 3 [Fig. 5(a)].

Sample 3 surface was imaged over a longer distance using image stitching from the edge all the way to 2 mm toward the sample center [Fig. 6(c)]. There is a pattern orientation change at around 1.1–1.4 mm from the edge. By superimposing the shear stress data (and its sign), the orientation change appears roughly around the simulated stress sign change (near 1.4 mm). Therefore, this result demonstrates the direct modulation (in amplitude and orientation) of surface patterns with shear stress. Finally, the stress values simulated in this zone suggest that a slight shear stress of the order of −0.1 MPa is enough to reverse the typical fracture deviation orientation observed on the reference sample 1.

IV. CONCLUSION AND PERSPECTIVES

With the help of a Smart Cut like process, shear stresses are voluntarily induced near the edges of bonded structures. The fracture study of such samples demonstrates the influence of local shear stress on the orientation and amplitude of the surface pattern on SOI substrates after the fracture step in the Smart Cut technology.

The origin of the typical SOI surface pattern for the fracture of a reference sample—without any induced stresses—is still under investigation. The main hypothesis could be the formation of slight shear stresses during fracture propagation in a material with asymmetric mechanical properties. Further investigations have to be conducted regarding buried oxide layer thickness and its impact on surface morphology.

Finally, this work opens up several perspectives. Indeed, it may be possible to control and improve the post-fracture surface roughness of SOI substrates by a defined global input of shear stress using an innovative process yet to be determined.

AUTHOR DECLARATIONS

Conflict of Interest

The authors have no conflicts to disclose.

Author Contributions

Lucas Colonel: Conceptualization (lead); Data curation (lead); Formal analysis (lead); Investigation (lead); Methodology (lead); Resources (lead); Software (equal); Validation (equal); Visualization (equal); Writing – original draft (lead); Writing – review & editing (lead). **Q. Lomonaco:** Conceptualization (equal); Data curation (equal); Formal analysis (supporting); Investigation (equal); Methodology (equal); Software (equal); Validation (equal); Writing – original draft (supporting); Writing – review & editing (equal). **K. Abadie:** Conceptualization (supporting); Data curation (supporting); Project administration (equal); Resources (equal); Supervision (equal); Writing – review & editing (equal). **L. G. Michaud:** Conceptualization (supporting); Methodology (equal); Project administration (equal); Resources (equal); Validation (equal); Visualization (equal); Writing – original draft (supporting); Writing – review & editing (equal). **C. Morales:** Data curation (supporting); Investigation (supporting); Methodology (supporting); Resources (equal); Supervision (supporting); Validation (supporting). **S. Moreau:** Conceptualization (supporting); Data curation (supporting); Investigation (supporting); Methodology (supporting); Software (lead); Supervision (equal); Validation (equal); Visualization (equal); Writing – original draft (equal); Writing – review & editing (lead). **F. Mazen:** Funding acquisition (equal); Investigation (supporting); Methodology (supporting); Project administration (equal); Resources (equal); Supervision (lead); Writing – original draft (supporting); Writing – review & editing (supporting). **F. Fournel:** Project administration (supporting); Resources (supporting); Software (equal); Supervision (lead); Validation (supporting); Visualization (supporting); Writing – original draft (supporting); Writing – review & editing (supporting). **D. Landru:** Funding acquisition (equal); Project administration (supporting); Resources (equal); Supervision (equal); Validation (supporting); Writing – original draft (supporting); Writing – review & editing (supporting). **F. Rieutord:** Conceptualization (supporting); Formal analysis (supporting); Investigation (supporting); Methodology (supporting); Project administration (equal); Supervision (lead); Validation (supporting); Writing – original draft (supporting); Writing – review & editing (supporting).

DATA AVAILABILITY

The data that support the findings of this study are available from the corresponding author upon reasonable request.

REFERENCES

[1]I. Issa *et al.*, Mater. Today **48**, 29–37 (2021).
[2]P. Gallo and A. Sapora, Appl. Sci. **10**, 1640 (2020).
[3]C. Wang *et al.*, Mater. Today Commun. **37**, 107542 (2023).
[4]M. Bruel, Electron Lett. **31**, 1201 (1995).
[5]G. K. Celler *et al.*, *Wafer Bonding Applications and Technology*, Springer Series in Materials Science (Springer, Berlin, 2004).
[6]Q.-Y. Tong and U. Gösele, *Semiconductor Wafer Bonding: Science and Technology* (John Wiley & Sons, New York, 1999).
[7]S. Personnic *et al.*, J. Appl. Phys. **103**, 023508 (2008).
[8]J. D. Penot *et al.*, J. Appl. Phys. **114**, 123513 (2013).
[9]L. Colonel *et al.*, Phys. Status Solidi A **218**, 2100219 (2021).
[10]A. Petit *et al.*, J. Appl. Crystallogr. **55**, 911–918 (2022).
[11]D. Landru *et al.*, Phys. Rev. Appl. **15**, 024068 (2021).
[12]D. Massy *et al.*, Appl. Phys. Lett. **107**, 092102 (2015).
[13]D. Massy *et al.*, Phys. Rev. Lett. **121**, 195501 (2018).
[14]Q. Lomonaco *et al.*, ECS Trans. **109**, 277 (2022).
[15]P. Nguyen *et al.*, J. Appl. Phys. **97**, 083527 (2005).
[16]T. Suga *et al.*, Acta Metall. Mater. **40**, S133–S137 (1992).
[17]C. Flötgen *et al.*, ECS Trans. **75**, 45 (2016).
[18]H. Takagi *et al.*, Appl. Phys. Lett. **68**, 2222 (1996).
[19]K. Abadie *et al.*, *Presentation at the WaferBond'19 Conference* (Fraunhofer Institute for Surface Engineering and Thin Films IST, Halle, 2019).
[20]Y. Okada and Y. Tokumaru, J. Appl. Phys. **56**, 314–320 (1984).
[21]G. Stoney, Proc. R. Soc. London, Ser. A **82**, 172 (1909).
[22]*Structural Mechanics Module. COMSOL Multiphysics®* (COMSOL, Stockholm, 2020), Vol. 5.6, pp. 75–84.
[23]Standard SEMI M1-0305 (SEMI, 2005).
[24]A. A. Griffith, Philos. Trans. R. Soc. A **221**, 163 (1921).
[25]F. Erdogan and G. C. Sih, J. Basic Eng. **85**(4), 519–525 (1963).
[26]H. Tada *et al.*, The Stress Analysis of Cracks Handbook (Del Research Corporation, 1973), Vol. 34, p. 635, ISBN-10 : 0791801535, ISBN-13 : 978-0791801536.